Crown Ether Covalent Organic Frameworks for Electrochemical Selective Alkali Metal Cation Capture

Dong Jiang[1,2], Jonathan P. Hill*[,3], Joel Henzie[3], Liang Feng[4], Liyang Zhu[1,2], Yingji Zhao[1,2] Toru Asahi[2], Ruibo Xu,[5] Xingtao Xu*[,5] and Yusuke Yamauchi*[,1,6,7]

[1]Department of Materials Process Engineering, Graduate School of Engineering, Nagoya University, Nagoya 464-8603, Japan. E_mail: y.yamauchi@uq.edu.au

[2]Faculty of Science and Engineering, Waseda University, 3-4-1 Okubo, Shinjuku, Tokyo, 169-8555, Japan.

[3]Research Center for Materials Nanoarchitechtonics, National Institute for Materials Science, 1–1 Namiki, Tsukuba, Ibaraki, 305-0044, Japan, E_mail: jonathan.hill@nims.go.jp

[4]Thomas Lord Department of Mechanical Engineering and Materials Science, Duke University, Durham, North Carolina, 27701, USA.

[5]Marine Science and Technology College, Zhejiang Ocean University, 316022, Zhoushan, China. E_mail: xingtao.xu@zjou.edu.cn

[6]Australian Institute for Bioengineering and Nanotechnology (AIBN), The University of Queensland, Brisbane, QLD 4072, Australia.

[7]Department of Chemical and Biomolecular Engineering, Yonsei University, Yonsei-ro, Seodaemun-gu, Seoul 03722, South Korea.

Abstract

Advances in separation processes, such as ion-capture electrodialysis, and related electrochemical technologies including electrochemical synthesis, fuel cells, and redox flow batteries, relies substantially on the development of high-selectivity ion capture materials. Covalent organic frameworks (COFs), characterized by their rigid structures, tunable functionalization, and well-ordered channels, offer a promising avenue for the next generation of electrochemical adsorptive materials. COFs hold immense potential for the optimization of various electrochemical processes based on active manipulation of the interplay between thermodynamic and kinetic selectivity. In this study, we present a novel approach employing covalent organic frameworks functionalized with a series of crown ethers for efficient and highly selective electrochemical capture of monovalent cations. Following optimization of synthesis conditions, a series of nanoflower-like COFs modified with different azacrown ether appendages was obtained. Crown ether moieties act as confining stages, imparting high selectivity for different monovalent cations depending on the cavity dimensions of crown ether present. COF-electrodes prepared using the novel crown-COFs exhibited superior performances for the selective sequestration of monovalent (alkali metal) cations. Notably, 18-crown-6 ether-substituted-COF shows a remarkable selectivity (14.26) of K^+ over Na^+, and a substantial Rb^+/Na^+ selectivity of 22.4. DFT calculations and MD simulations suggest that the unexpectedly high selectivity for larger cations is likely due to diverse binding modes, in conjunction with the porous structure of the COFs. Given their lower dehydration free energies and smaller hydrodynamic radii, K^+, Rb^+, and Cs^+ more readily permeate the COF channels. In contrast, Na^+ and Li^+, with significantly higher dehydration free energies and hydrodynamic radii, diffuse into the crown-COF structure at a much slower rate and are bound predominantly at the surfaces of the COF particles.

Introduction

Materials capable of selective sequestration of monovalent cations, especially alkali metal cations, are essential for energy storage and conversion applications[1]. There is burgeoning interest in these materials based on possible uses in ionic batteries[2], energy-efficient separation/purification processes,[3] and electrochemical applications including CO_2 reduction[4], direct water electrolysis, ion-capture electrodialysis[5], amongst others[6,7]. In all these electrochemical applications, whether emerging or already well-established, materials that selectively sequester cations can serve as electrode components forming favorable cation-layers during electrochemical processes, or can be used as membrane separators enabling the selective transfer of target cations to designated device regions concurrently rejecting undesirable cationic species.[3,5] Ultimately, ion selectivity of these materials originates from Ångstrom-scale filters due to the established mechanism involving size (steric) effects, Donnan (charge) exclusion, and dielectric exclusion.[8] However, the separation of mixtures of monovalent cations is strongly hindered by uniformity of monovalency, subnanometer cation dimensions (i.e., 1.0–3.0 Å for non-hydrated cations, 6.4–8.0 Å for hydrated ions), and only Å-level variation (< 2 Å) in the sizes of the cations.[9,10] Cation dehydration or chemical recognition have both been recently proposed as potential mechanisms to control the selective capture or transport of ions under sub-nanometer confinement in porous materials.[10] However, the deep structure-function relationship behind the sequestration of ions within sub-nanometer channels remains obscure. Therefore, there is a rapidly emerging demand for the synthesis of materials having precisely tunable chemical environments at channel interiors promoting the selectivity towards targetable monovalent cations.[12]

Organic materials containing designable functional groups dominate current selective ion-transport materials used for practical purposes at all scales, due to their low cost and manufacturing scalability.[7,13-15] Crown ethers are a class of ligands known to bind various cations depending, in part, on the relative size of their cavity and the size of the target cation.[16,17] For example, 12-crown-4 ether (12C4) forms reversible complexes with both Na^+ and Li^+ cations, where the relative affinity depends on the chemical environment and sub-nanometer engineering.[18] Selective Li^+ transport involving crown ethers incorporated into liquid membranes has been reported.[19] However, these crown ethers are not chemically bound to the membrane and can leach into solution during the process. Other studies have involved grafting of crown ethers onto a polymer substrate in attempts to achieve cation-specific selectivity. Unfortunately, these materials are poorly defined and can undergo severe swelling, which might facilitate ion diffusion but can also cause reduced selectivity. An emerging philosophy of synthesis suggests limiting the dimensions of pore voids by increasing the rigidity of polymer backbones, which reduces the thermal motion of the polymer segments. This is thought to enforce size selectivity and improve long-term separation performance. Other strategies have involved the assembly of crown ether molecules in the channels of metal organic frameworks (MOFs). For example, in the case of MOFSNC, the specific binding of Na^+ cations by 15C5 confined in its rigid sub nanochannel leads to a permeation rate sequence of $Na^+ >> K^+ > Li^+$ and a high Na^+/K^+ selectivity.[20] While MOFs can provide rigid channels for crown ethers, the typically used post-synthetic introduction of crown ethers makes the precise control of their quantity and locations within the channels challenging.[20] MOFs also exhibit poor stabilities under many

conditions, including high temperature or at non-neutral pH. Therefore, the development of CE-based materials for selective capture of monovalent cations under precise chemical conditions and structural control holds significant appeal.[21]

Covalent organic frameworks (COFs), characterized by their adjustable structure, well-ordered channels and high chemical and thermal stability, offer a promising avenue for the next generation of electrochemically-active adsorptive materials.[22-24] Their long-range ordered structures impart narrow distributions of channel dimensions ensuring substantial cation sieving effects. The channel size of COFs can be carefully tailored in the range of 0.5 – 10.0 nm through the rational screening of linker and linkages, leading to greater freedom in channel construction towards target cation separations.[25,26] Moreover, COFs can accommodate abundant and homogeneously dispersed functional groups for better control over multiple physicochemical interactions promoting stronger recognition towards the targeted cations.[27,28] The successful introduction of crown ether into COF channels has been reported either as branched functional groups or as a component of the COF framework. Those materials have been applied in phase transfer reactions, as fluorescence sensors, etc.[29,30] However, the efficient construction of COF-based CEs with high crystallinity and controlled morphology remains a challenge, and the use of COFs for monovalent alkali metal cation adsorption and separation is still in its infancy.

Herein, a new series of crown ether functionalized units (with 12-crown-4 (NC12), 15-crown-5 (NC15), 18-crown-6 (NC18) ethers), that are 2’-crown-ether-substituted-[1,1':4',1''-terphenyl]-4,4''-dicarbaldehydes, were designed and synthesized as struts for the construction of three new COFs bearing crown ethers as branched groups. Crown-

COF synthesis involves Schiff base reaction with 1,3,5-tris(4-aminophenyl)benzene (TAB). The effects of liquid additive and catalyst on the reaction and product formation were investigated, revealing pronounced effects on COF formation, affecting both the crystallinity of the products, their yields, as well as their morphologies. After optimization of the reaction conditions, a family of nanoflower-like crown ether COFs was obtained. The electrodes prepared using the resulting COFs exhibit superior performance for the selective capture of monovalent cations. Notably, the NC18-TAB COF showed a large selectivity of K^+ over Na^+ at 14.26, and a large Rb^+/Na^+ selectivity of 22.4 among these NCx-TAB-COFs.

Results and Discussion

Synthesis and Characterization. A schematic illustration of the synthesis of this series of crown ether-based COFs is shown in **Fig. 1a** (see also Scheme S1)**.** The NCx-TAB COFs (X = 12 for 12C4, 15 for 15C5, and 18 for 18C6) were respectively constructed by condensing NC12-macTP-CHO_2, NC15-macTP-CHO_2, or NC18-macTP-CHO_2 with TAB in a solvent mixture (a 1:4 v/v of 1,2-dichlorobenzene and 1-butanol) in the presence of a catalyst (scandium tris(trifluoromethanesulfonate), $Sc(OTf)_3$) under solvothermal conditions. The resulting insoluble crown-COF materials were characterized using different spectroscopic techniques. To confirm Schiff-base polymerization, Fourier transform infrared (FTIR) spectra of the COFs obtained from typical starting dialdehydes (NC18-macTP-CHO_2) and TAB are shown in **Fig. 1b**. The aldehyde C=O(str.) band of NC18-macTP-CHO_2 at 1700 cm^{-1} as well as the sharp N-H(str.) band of TAB at 3372 cm^{-1} are

eliminated after Schiff-base reaction. The imine C=N (str.) of the COF emerges as expected at around 1625 cm^{-1} although it overlaps with amide C=O (str.) and aromatic C=C (str.) bands of the crown sidechain and the terphenyl units, respectively. Any residual absorption at 1700 cm^{-1} in the FTIR of the COFs is probably due to moisture included in the pores.[29] ^{13}C cross-polarization (CP) magic-angle spinning nuclear magnetic resonance (CP-MAS NMR) was also performed to confirm the formation of the COFs (**Fig. 1c**). Taking NC12-TAB COF, for example, the peak at 159 ppm is attributed to the carbon of the C=N bond. Peaks at 71 and 74 ppm are assigned to carbon atoms of crown ethers units, and the other intense resonance signals at 100–152 ppm originate from aromatic carbon atoms of the phenyl rings.[29] Peaks around 20 and 225 ppm are spinning sidebands.[31] Similar spectra were obtained for NC15-TAB COF and NC18-TAB COF.

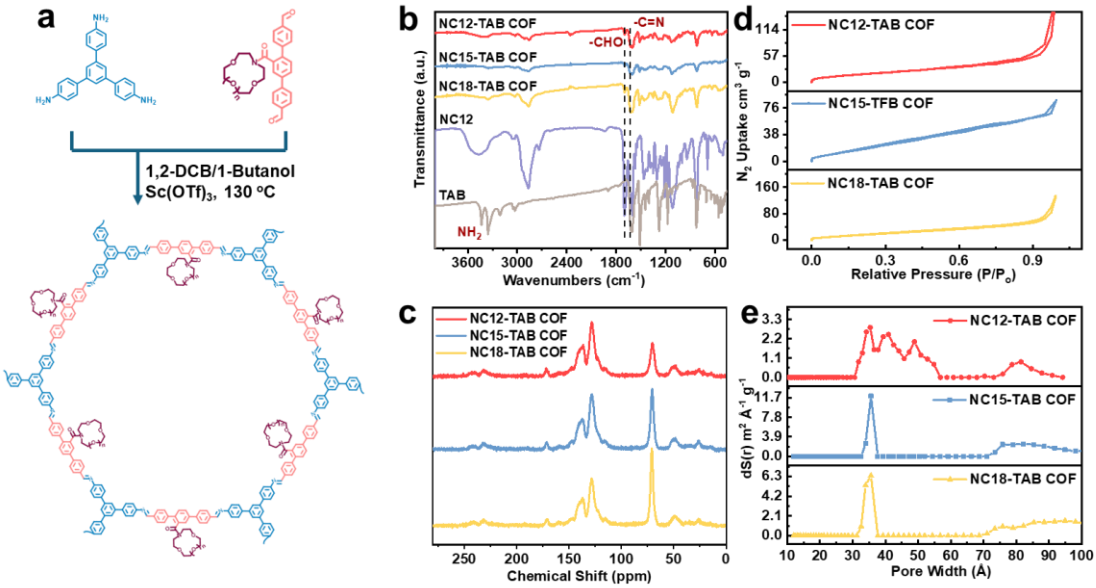

Fig. 1. Design and synthesis of NCx-TAB COFs. **a**, Synthesis of NCx-TAB COF. **b**, FTIR spectra of the NCx-TAB COF building blocks and the NCx-TAB COFs. Note the similarity of the spectra of COFs. **c**, ^{13}C CP-MAS spectra of the NCx-TAB COFs. **d**, Nitrogen sorption isotherms for NCx-TAB COFs measured at 77 K. **e**, Pore size distribution profiles of NCx-AFB COFs derived from nitrogen sorption data.

Ordered porous structure is another important feature of COFs. The permanent porosity of these COFs was studied by N_2 isotherm at 77 K. All three COFs show Type IV isotherms with relatively low adsorption suggesting mesoporous structures of the materials (**Fig. 1d**). The Brunauer-Emmett-Teller (BET) surface areas for NC12-TAB COF, NC15-TAB COF and NC18C-TAB COF were calculated to be 44.12, 44.19 and 38.25 $m^2\ g^{-1}$, respectively. It has been observed in other cases that the crown ether units obstruct pores to some extent, interfering with N_2 adsorption in the BET technique, resulting in relatively low specific surface areas of the materials.[32,33] Pore size distributions were calculated from N_2 adsorption data by using the DFT method and revealed that NCx-TAB COFs are mesoporous with pore sizes around 3.54 nm for NC12-TAB COFs (**Fig. 1e**) The pore size is close to the simulated value (5.3 nm) with the difference probably being due to a combination of disorder in the polymer framework and distortion of the flexible crown ether moieties upon solvent removal.[29,33] These data demonstrate the successful preparation of NCx-TAB COFs as porous imine framework polymers.

The high crystallinity of the crown-COFs is confirmed by the presence of sharp diffraction peaks in the small angle region of their powder X-ray diffraction patterns (pXRD; **Fig. 2**). Considering the geometry of the precursors, the connection patterns and a layered morphology observed by SEM and TEM, 2D topologies of the materials are expected. A structural model based on a 2D network structure with an AA stacking mode for NCx-TAB-COFs **(Fig. 2)** gave the following unit cell parameters for the structures: a = 52.4 Å, b = 52.4 Å, c = 3.6 Å, α = 90°, β = 90°, and γ = 120°). The experimental pXRD pattern for NCx-TAB exhibited two main diffraction peaks at around 2.2° and 20.0° assigned respectively to

the (100) and (001) reflections. The experimental pXRD patterns **(Fig. 2a-c)** are in good agreement with the simulated patterns based on an AA stacking structure of NCx-TAB COFs **(Fig. 2b-h)** suggesting that the materials consist of an eclipsed porous structure. The lattice modeling and Pawley refinement (Materials Studio, version 7.0) provide excellent agreement factors, with unit cell parameters a = 52.49 ± 0.0438, b = 52.43 ± 0.044, c = 3.59 ± 0.003, α = 90.027 ± 0.0068, β = 90.0005 ± 0.0097, γ = 120.1119 ± 0.003 for NC12-TAB COF (R_{wp} = 4.24 %, R_p = 3.2 %), a = 52.44 ± 0.0625, b = 52.46 ± 0.0671, c = 3.58 ± 0.0045, α = 90.0048 ± 0.0100, β = 90.0360 ± 0.0069, γ = 120.0380 ± 0.0037; for NC15-TAB COF (R_{wp} = 2.65 %, R_p = 1.91 %), and a = 52.458 ± 0.2577, b = 52.449 ± 0.2540, c = 3.5842 ± 0.01756, α = 89.925 ± 0.0123, β = 90.0372 ± 0.0177, γ = 119.8825 ± 0.0120 for NC18-TAB COF (R_{wp} = 3.48 %, R_p = 2.05 %), after optimization. The crown-COF materials were also examined using high-resolution transmission electron microscopy (HR-TEM) to assess any long-range ordered internal structures. As shown in **Fig. 2g-i**, a combination of pores and layered structures can be observed in face-on and edge-on directions for NC12-TAB COF, NC15-TAB COF and NC18-TAB COF, further confirming their ordered structures.

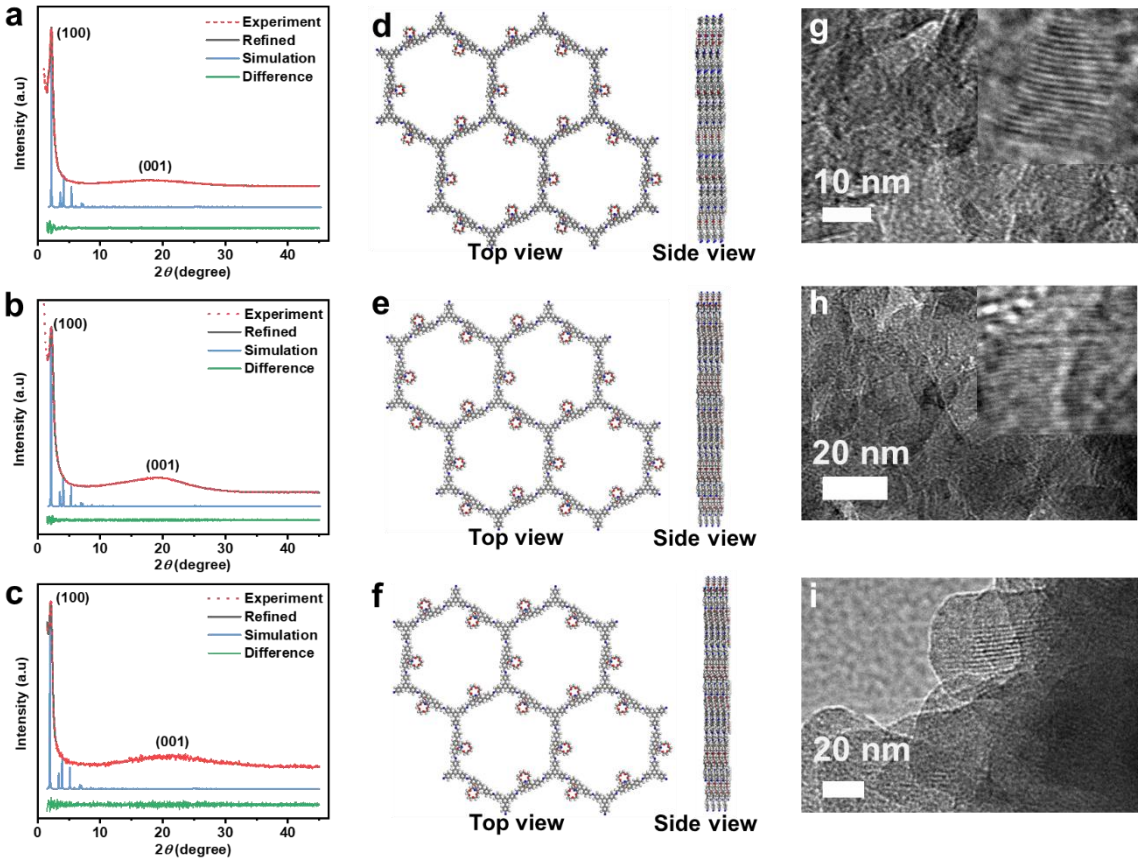

Fig. 2. Powder XRD patterns and HR-TEM images of crown-COFs. Experimental (red), the simulated patterns for eclipsed AA stacking mode (blue) of **a**, NC12-TAB COF, **b**, NC15-TAB COF, and **c**, NC18-TAB COF. Model AA stacking crystal structure of top and side views of **d**, NC12-TAB COF, **e**, NC15-TAB COF, and **f**, NC18-TAB COF; TEM images: **g**, NC12-TAB COF, h, NC15-TAB COF, and **i**, NC18-TAB COF.

Crown-COF Morphology Control. As mentioned previously, the optimized reaction for the construction of NC-TAB COFs with a uniform nanoflower morphology involves using a solvent mixture (1:4 v/v 1,2-dichlorobenzene:1-butanol) and $Sc(OTf)_3$ as a Lewis acid catalyst under solvothermal conditions. Solvent system, catalyst and reaction temperature are all critical in the control of product morphology and yield, and for the optimization of crystallinity. Taking the synthesis of NC18-TAB COF as an example, three different solvent mixtures were applied with other conditions (concentration, temperature, catalyst) fixed, to

assess morphology control by this method (see **Table 1**). Mesitylene/dioxane yielded a spherical particulate morphology with diameters in a wide range from 1.3 to 8 μm while *N*,*N*-dimethylformamide/dioxane gave an aggregated particle morphology. A homogeneous nanoflower-like morphology of NC18-TAB COF with uniform particles of 1 μm diameter could be obtained only in 1,2-dichlorobenzene/1-butanol. Solvent-based morphology control arises due to different solvent-microcrystal interactions during the reaction.[34] COF yield is also improved (to ~30% from ~10%) in this solvent mixture. The yield was further improved by optimizing the catalysts where the strong Lewis acid $Sc(OTf)_3$ increased the yield of NC18-TAB COF from ~30% (Cat: acetic acid) to ~80% with a concurrent improvement in crystallinity of the product.[35] We also studied the effect of temperature on product morphology where NC18-TAB COF products obtained at 50 °C had a nanoscale sheet-like morphology without assembly into a nanoflower sphere. At higher temperature (130 °C), intermediates are subjected to higher diffusion rates and greater surface energy leading to the formation of multiple nuclei during growth and rapid branching, resulting in nanoflower-like structures. Under similar reaction conditions, NC12-

TAB COF and NC15-TAB COF also resulted in nanoflower morphology. (**Fig. S1-S3)**

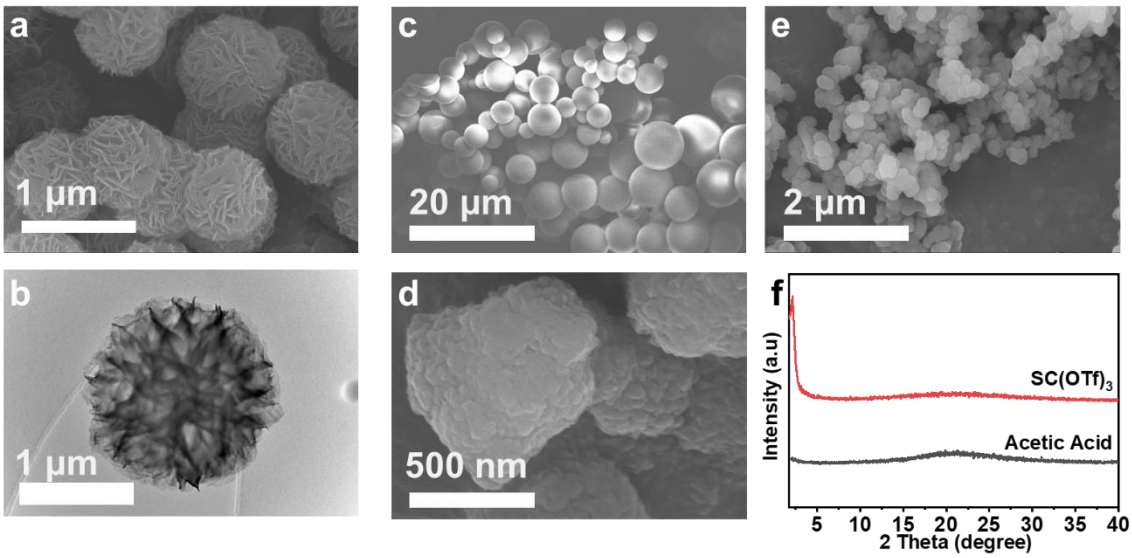

Fig. 3. Morphology control experiments. **a**, SEM and **b**, TEM images of NC18-TAB COF prepared using 1,2-DCB/1-butanol (1:4 v/v) as solvent with $Sc(OTf)_3$ as the catalyst at 130 °C. SEM images of NC18-TAB COF using **c**, mesitylene/dioxane or **d**, DMF/dioxane as solvent and acetic acid as catalyst at 130 °C. **e**, SEM image of NC18-TAB COF obtained using 1,2-DCB/1-butanol as solvent and $Sc(OTf)_3$ as catalyst at 130 °C. **f**, Powder XRD patterns of NC18-TAB COF obtained using acetic acid (black) or $Sc(OTf)_3$ (red) as catalyst.

Table 1 Optimization of the reaction condition for making NCx-TAB-COF with controlled solvent, temperature and catalyst.

Solvent	**Temperature and Catalyst**	**Yield**
Mesitylene / Dioxane	**Temperature:** 130 ºC **Catalyst:** 6 M Acetic Acid	< 10%
DMF / Dioxane		< 10%
1,2-DCB / 1-Butanol		~30% (the yield can reach 80% when using $Sc(OTf)_3$ as catalyst)

Selective sequestration performance for alkali metal cations

Given the high density of CEs in the skeleton of these COFs and their highly ordered porous structures, we have assessed their use for electrochemical capture of alkali metal ions. For proof-of-concept, an asymmetric capacitive deionization configuration with NCx-TAB COFs as cathode (for alkali metal ion capture) and activated carbon (AC) as the anode (for chloride anion capture), was constructed (for a schematic see Figure S. Compared to symmetric configurations, asymmetric electrode configurations facilitate ion capture performance due to larger safe operating voltages and greater flexibility in the choice of electrode materials.[36] During the electrochemical ion capture process, no bubbles of gas could be observed, indicating that side reactions such as chlorine generation or water splitting were absent. The concept of the potential process for selective ion capture is illustrated in **Fig. 4a**. It is well known that crown ethers can serve as hosts for binding of target cations due to their macrocyclic cavities and multiple electron-donating ligand valency. Functional group modification (in this case introduction of an amide) or the introduction of heteroatoms into the ring can alter its selective adsorption properties. Typical selectivity trends can also be reversed when ion dehydration effects or ion-pore-wall interactions become significant.[18] Crown ethers with different multiplicity of oxygen atoms have different solvation capabilities and flexibility. Therefore, varying the type of crown ethers (multiplicity of O atoms) within the pore channel should enable the optimization of energy differences between cations captured in the materials leading to enhanced selectivity of adsorption for targeted ions with concurrent exclusion of others.[37] In this case, the NCx-TAB COF series have no effective capacity Li^+ ions (data excluded).

However, as shown in **Fig. 4b-d**, NC12-TAB COF exhibits selectivity for alkali metal cations in the order $K^+ > Rb^+ > Cs^+ > Na^+$, with a capacity of 2.91, 1.71, 0.99, and 0.66 mmol g^{-1}, respectively. For the NC15-TAB COF, selectivity is modulated in the order $Rb^+ > K^+ > Cs^+ > Na^+$, with respective capacities of 2.64, 1.96, 1.55, and 0.49 mmol g^{-1}. For NC18-TAB COF, selectivity arises in the order $Rb^+ > Cs^+ > K^+ > Na^+$ with capacities of 2.24, 1.82, 1.43, and 0.10 mmol g^{-1}, respectively. Notably, the NC18-TAB COF shows the highest selectivity of K^+ over Na^+ with a selectivity of 14.26, and the highest Rb^+ / Na^+ selectivity of 22.4. Considering the cations, K^+ and Na^+ exhibit a decreasing trend in capacity with respect to the size of crown ether rings, while the Cs^+ cations display a contrary tendency. For Rb^+, the highest capacity for sequestration is found for NC15-TAB COF.

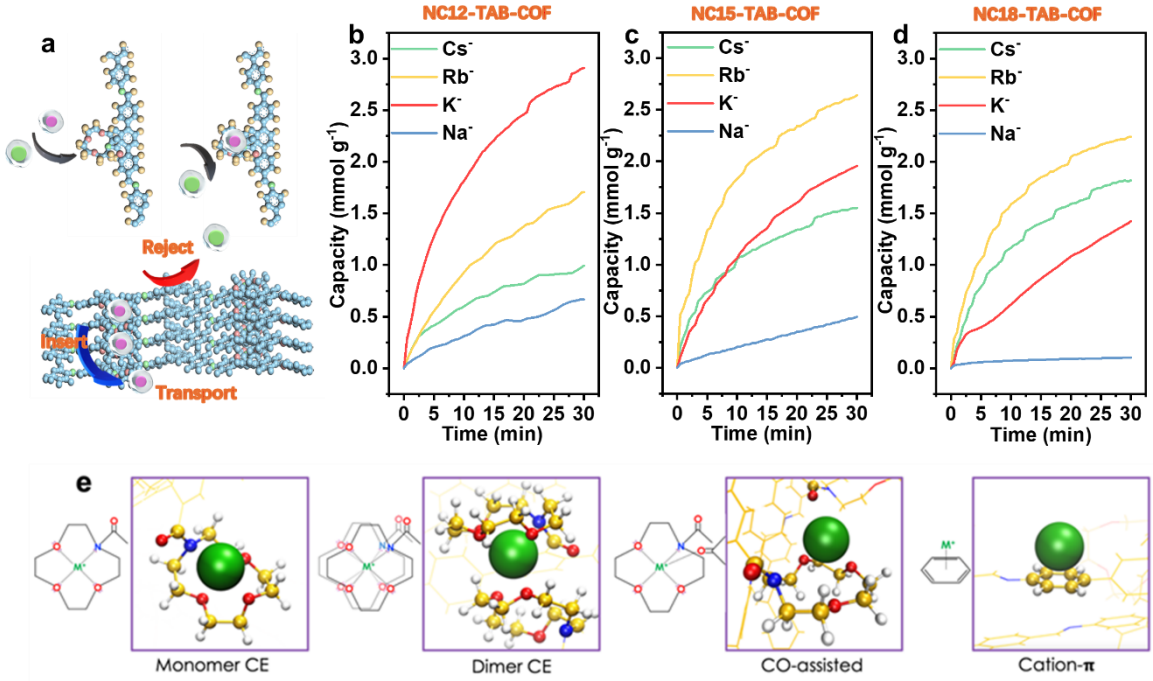

Fig. 4. Electrochemical alkali metal cation sequestration by NCx-TAB COFs. **a**, Proposed potential selective capture mechanism. Electrochemical selective alkali metal cation capture performance of **b**, NC12-TAB COF, **c**, NC15-TAB COF, and **d**, NC18-TAB COF. **e**, Binding modes of M^+ and COFs estimated using density functional theory (DFT) calculations (see Supplementary Information, Section 5 for details).

Mechanism of selective alkali metal cation capture

The above tendencies of alkali metal cation binding appear to deviate from the expected intrinsic ion binding affinity of the crown ethers. For example, 12-crown-4 ether, which has a cavity size similar to NC12, typically favors Li^+ over other larger cations.[38] This suggests that the ion-capture mechanism by NCx-TAB COFs may not be governed solely by the interaction between the cations and the electron-donating atoms of individual crown ether macrocycles, potentially involving more complex binding modes. Therefore, theoretical calculations were performed to explore possible modes of cation capture by NCx-TAB COFs. First, density functional theory (DFT) calculations were employed to calculate the dissociation free energies of the cation–crown ether complexes (see **Table S1**), denoted as $M^+ \in NCx$ (x = 12, 15, 18 with $\Delta G = G_{M+} + G_{NCn} - G_{M+\in NCn}$). The results highlight the strong binding of Na^+ to all of the crown ethers, with dissociation free energies of 5.3, 9.5, and 19.5 kcal mol^{-1} in the $Na^+ \in$ NC12, $Na^+ \in$ NC15, and $Na^+ \in$ NC18 complexes, respectively. This suggests that if the binding mechanism were governed solely by the interaction between M^+ and lone pairs of a single crown ether ring, Na^+ should exhibit the strongest binding.

Molecular dynamics (MD) simulations were also performed to further investigate the capture mechanism of cations involving multiple crown ethers (see Supplementary Information, Section 6 for details). The MD simulation results validate the DFT findings in that Na^+ binds strongest to the crown ethers, since the predominant binding mode of cations involves only one crown ether (monomer CE mode, see **Fig. 4e**). However, we also identified binding modes involving two crown ethers (dimer CE mode) and an alternative

mode, where M^+ interacts with oxygen atoms of one crown ether and the amide carbonyl group of another crown ether in close proximity (C=O-assisted mode). Finally, since COFs consist of a large number of electron-rich aromatic moieties, cation–π interactions might also play a role in the ion-capturing process.[39, 40]

Based on the evidence obtained from DFT calculations and preliminary MD simulations, we hypothesize that the unexpectedly higher selectivity of larger cations could be linked to the porous structure of the particles. Given their lower dehydration-free energies and smaller hydrodynamic radii,[41] K^+, Rb^+, and Cs^+ permeate more easily through the nanoflower particles with smaller pore sizes. Conversely, Na^+ and Li^+ have significantly higher dehydration-free energies and hydrodynamic radii, so that they diffuse into the porous structure at a much slower rate being captured predominantly at the surface of the particles (so occupying fewer binding sites).

Conclusion

In conclusion, we have successfully synthesized a series of COFs containing different crown ether moieties as branched groups using an optimized imine condensation reaction. The resulting NCx-COFs were used for the electrochemical separation of alkali metal ions. This represents a new efficient method for the synthesis of imine-linked crystalline COFs containing crown ethers as side chains, with the materials exhibiting good crystallinity in a controlled nanoflower-like morphology. The resulting COF-electrodes demonstrate superior performances in the selective sequestration of alkali metal cations. Notably, NC18-TAB COF showed a high selectivity of K^+ over Na^+ at 14.26 and a high Rb^+ / Na^+

selectivity of 22.4. Our results demonstrate that COFs offer a powerful platform for the precise design of synthetic cation absorbents with unprecedented selectivity based on the integration of crown ether units.

Competing Interests

The authors declare that there are no competing interests.

Author contributions

Data Availability

Data relevant to this work are given in the Supplementary Information. Supplementary Figures 7–30 contain chemical analytical data for the COF precursors.

Acknowledgements

This work was partly supported by World Premier International Research Center Initiative (WPI Initiative), MEXT, Japan. The authors are also grateful to JST-ERATO Yamauchi Materials Space- Tectonics Project (JPMJER2003) and the Queensland Node of the Australian National Fabrication Facility (ANFF-Q).

Methods

Chemicals and reagents

Reagents and dehydrated solvents (in septum-sealed bottles) used for syntheses and spectroscopic measurements were purchased from Tokyo Kasei Chemical Co., Wako Chemical Co., Nacalai Tesque Chemical Co. or Aldrich Chemical Co. and were used as received. Silica gel for chromatographic separations was obtained from Wako Chemical Co. Ltd. (Silica gel 60N, spherical, neutral, particle size 63 – 210 μm).

Synthesis of NCx-TAB COFs

Synthesis and characterization of COF precursors are given in the Supplementary Information. NCx-TAB COFs (X = 12 for 12C4, 15 for 15C5, 18 for 18C6) were synthesized by condensing the respective NCx-macTP-$(CHO)_2$ with 1,3,5-tris(4-aminophenyl)benzene (TAB), in a solvent mixture (1,2-dichlorobenzene : 1-butanol, 1 : 4 v/v) using scandium tris(trifluoromethanesulfonate) as a Lewis acid catalyst under solvothermal conditions.

Characterization

Powder X-ray diffraction patterns were recorded using a Rigaku SmartLab diffractometer equipped with a Cu anode X-ray source (40 kV, 15 mA) in standard Bragg-Brentano geometry. Nitrogen gas adsorption-desorption isotherms of the porous polymers were measured using an automatic adsorption instrument (Quantachrome Instruments, Autosorb-iQ2, USA) at liquid nitrogen temperature (77.35 K). Patterns were recorded in the range 2–80 degrees 2θ at a scan rate of 4 deg. min^{-1}. SEM images were collected using an S-4800 FE-SEM (Hitachi, Japan) operated at an accelerating voltage of 10 kV.

Transmission electron microscopy (TEM) was performed using a JEM-2100F instrument (JEOL, Japan) operated at 200 kV. Pore size distributions were calculated from the adsorption branches of the isotherms using a nonlocal density functional theory (DFT) method.

Electrochemical selective cation capture performance.

Selective alkali metal ion capture properties of the three COFs were conducted using a capacitive deionization cell consisting of the NCx-TAB COFs cathode, an activated carbon (AC) anode, an anion exchange membrane (AEM), and a cation exchange membrane (CEM) (Supplementary Figure 4). All electrodes were prepared as follows: active material, super P and PVDF in a weight ratio of 70 % : 20 % : 10 % were mixed in N-methylpyrrolidone (NMP) to form a slurry. The slurry was then dropped onto graphite paper (2.5 cm^2 × 2.5 cm^2) and dried at 60 °C for 12 h. Batch-mode desalination experiments were conducted in aqueous alkali metal chloride salt solution with a continuous recycling system, including a CDI apparatus, a peristaltic pump, a power source, and a tank. In each experiment, the real-time saline concentration, current, and pH variation were monitored and measured at the outlet of the CDI apparatus. The volume of the saline solution was fixed at 30 mL and the operating voltage was 1.5 V. The duration of each half-cycle was 30 min to ensure near-equilibrium conditions. The cation adsorption capacity (IAC (M^+), mg g^{-1}) at t min was calculated using the following equations:

$$IAC\ (M^+) = (C_0 - C_t) \times V \times M_M^+/(m \times M)$$

$$IAR(M^+) = IAC(M^+)/t$$

where C_0 and t are the concentrations of MCl (M = Na, K, Rb, and Cs) at the initial stage

and t min, respectively, V is the volume of the MCl solution (L), m is the mass of the active materials (mg), M is the molar mass of MCl and M_{M+} is the molar mass of M^+.

Dissociation free energy of M^+-crown-ether

Density functional theory (DFT) calculations and molecular dynamics (MD) simulations were performed to study the binding (or dissociation) of alkaline cations M^+ (Li^+, Na^+, K^+, Rb^+, Cs^+) to three crown ethers NC12, NC15, and NC18. The dissociation free energies ($\Delta G = G_{M+} + G_{\text{crown ether}} - G_{M+\in\text{crown ether}}$) of M^+ from the three crown ethers were calculated with DFT implemented in the Turbomole software package.[42-43] All optimized structures in the gas phase were obtained at the PBE-D3(BJ)/def2-SVP level of theory.[45-46] The character of the optimized structures and quasi-harmonic Gibbs free energy corrections were characterized by subsequent frequency calculations. On top of the optimized structures, single-point calculations with B3LYP-D3(BJ)/def2-TZVP were done.[47-50] The implicit COSMO solvation model was used to account for the water environment.[51] Here, we employed models consisting of **NC12-macTP**, **NC15-macTP**, and **NC18-macTP** segments of the COFs. We deemed that these models are sufficiently large to correctly describe the binding of alkaline cations to the crown ethers.

Optimized structures of the cation–crown ether complexes, denoted as $M^+ \in$ NC12, $M^+ \in$ NC15, and $M^+ \in$ NC18, are shown in Supplementary Figure 5. The average bond distances between M^+ and the ether oxygen atoms, as well as the M^+ – nitrogen distances, are shown in Supplementary Table 2. The total energies (in E_h) of cations (Supplementary Table 3)[52], total energies (in E_h) of NC12 and $M^+ \in$ NC12 (Supplementary Table 4), total energies (in E_h) of NC15 and $M^+ \in$ NC15 (Supplementary Table 5), and total energies (in

E_h) of NC18 and $M^+ \in$ NC18 (Supplementary Table 6) are also presented in Supplementary Information.

MD simulations of $M^+ \in$ NC12, $M^+ \in$ NC15, and $M^+ \in$ NC18 complexes

To investigate the stability of M+ ∈ NC complexes, MD simulations with multiple crown ethers were performed using the Gromacs software package.[53] The models are shown in Supplementary Figure 6. Each model includes five COF layers, with each layer containing 18 crown ethers. An AA stacking structure was employed. Initially, we introduced 90 alkaline cations between the crown ethers. The simulation box was then neutralized with 90 Cl− anion and solvated with ~180,000 TIP3P water molecules.[54] This results in a simulation box containing more than 500,000 atoms. The OPLS-AA force field was used,[55] with the aid of the PolyParGen web server.[56-58] Energy minimization was performed using the steepest descent method with a threshold for the maximum force of 100.0 kJ mol^{-1} nm^{-1}. Long-range electrostatic interactions were treated using the fast smooth Particle-Mesh Ewald (PME) technique, with fourth-order cubic interpolation and a grid spacing of 0.16 nm.[59-60] Both short-range electrostatic cut-off and Van der Waals cut-off were set to 1 nm. NVT and NPT equilibration steps of 400 ps were then performed at T = 300 K and p = 1 atm. A value of 2 fs was used as the time step for integration. The V-rescale thermostat[61] was used with a coupling time of 0.1 ps, whereas the C-rescale barostat[62] with a coupling time of 2.0 ps was employed. The LINCS algorithm was employed to constrain bonds with hydrogens.[63] Finally, a short NPT production run of 40 ns was conducted. In the last snapshot of the simulation, we analyzed the number of ions captured by the crown ethers,

which should correlate with the M^+–crown ether dissociation energy. The last snapshots of the simulations are depicted in Supplementary Figure 6.

References

1. Zhou, X. et al. Intrapore energy barriers govern ion transport and selectivity of desalination membranes. *Sci. Adv.* **48,** eabd9045 (2020).
2. Razmjou, A., Asadnia, M., Hosseini, E., Habibnejad Korayem, A. & Chen, V. Design principles of ion selective nanostructured membranes for the extraction of lithium ions. *Nat. Commun.* **10**, 5793 (2019).
3. Zhang, H. Ultrafast selective transport of alkali metal ions in metal organic frameworks with subnanometer pores. *Sci. Adv.* **2,** eaaq0066 (2018).
4. Xu, K., Li, J., Liu, F., Chen, X., Zhao, T., & Cheng, F. Favoring CO intermediate stabilization and protonation by crown ether for CO_2 electromethanation in acidic media. *Angew. Chem. Int. Ed. Engl.* **62**, e202311968 (2023).
5. Uliana, A., Bui, N., Kamcev, J., Taylor, M., Urban, J. J., & Long, J. J. Ion-capture electrodialysis using multifunctional adsorptive membranes. *Science* **6539,** 296-299 (2021).
6. Yan, G. et al. The role of solid solutions in iron phosphate-based electrodes for selective electrochemical lithium extraction. *Nat. Commun.* **13**, 4579 (2022).
7. Liu, X. et al. Efficient and selective capture of thorium ions by a covalent organic framework. *Nat. Commun.* **14**, 5097 (2023).
8. Wang, H. et al. Covalent organic framework membranes for efficient separation of monovalent cations. *Nat. Commun.* **13**, 7123 (2022).
9. Hou, J., Zhang, H., Simon, G. P. & Wang, H. Polycrystalline advanced microporous framework membranes for efficient separation of small molecules and ions. *Adv. Mater.* **32**, e1902009 (2020).
10. Lu, J., Hu, X., Ung, K. M., Zhu, Y., Zhang, X. & Wang H. Metal–organic frameworks as a subnanometer platform for ion–ion selectivity. *Acc. Mater. Res.* **3**, 735-747 (2022).
11. Zuo, P. et al. Near-frictionless ion transport within triazine framework membranes. Nature 617, 299-305 (2023).
12. Lu, J. et al. Efficient metal ion sieving in rectifying subnanochannels enabled by metal-organic frameworks. *Nat. Mater.* **19**, 767-774 (2020).
13. Yuan, Y. et al. Selective scandium ion capture through coordination templating in a covalent organic framework. *Nat. Chem.* **15,** 1599–1606 (2023).
14. Tan, R. et al. Hydrophilic microporous membranes for selective ion separation and flow-battery energy storage. *Nat. Mater.* **19**, 195-202 (2020).
15. Feng, L. et al. Ultrasensitive and highly selective detection of strontium ions. *Nat. Sustain.* **6,** 789-796 (2023).
16. Poe, T. N. et al. Isolation of a californium (II) crown-ether complex. *Nat. Chem.* **15,** 722-728 (2023).
17. Shen, J. C. et al. A Rings-in-pores net: crown ether-based covalent organic frameworks for phase-transfer catalysis. *Chem. Commun.* **56**, 595-598 (2020).

18. Warnock, S. J. et al. Engineering Li/Na selectivity in 12-Crown-4-functionalized polymer membranes. *PNAS* **118,** e2022197118 (2021).
19. Barboiu, M. Encapsulation versus self-aggregation toward highly selective artificial K^+ channels. *Acc. Chem. Res.* **51**, 2711-2718 (2018).
20. Jun L. et al. An artificial sodium-selective subnanochannel. *Sci. Adv.* **9,** eabq1369 (2023).
21. Ye, T. et al. Artificial sodium-selective ionic device based on crown-ether crystals with subnanometer pores. *Nat Commun* **12**, 5231 (2021).
22. Vazquez-Molina, D. A. et al. Mechanically shaped 2-dimensional covalent organic frameworks reveal crystallographic alignment and fast Li-ion conductivity. *J. Am. Chem. Soc.* **138,** 9767-9770 (2016).
23. Wang, S. et al. Exfoliation of covalent organic frameworks into few-layer redox-active nanosheets as cathode materials for lithium-ion batteries. *J. Am. Chem. Soc.* **139**, 4258-4261 (2017).
24. Kandambeth, S. et al. Covalent organic frameworks as negative electrodes for high-performance asymmetric supercapacitors. *Adv. Energy Mater.* **10,** 2001673 (2020).
25. Sheng, F. et al. Efficient ion sieving in covalent organic framework membranes with sub-2-nanometer channels. *Adv. Mater.* **33**, e2104404 (2021).
26. Wang, C. et al. Ion-selective covalent organic frameworks boosting electrochemical energy storage and conversion: A review. *Energy Storage Materials* **55**, 498-516 (2023).
27. Liu, C. et al. A half-wave rectified alternating current electrochemical method for uranium extraction from seawater. *Nat. Energy* **2,** 17007 (2017).
28. Cheng, K., Li, H., Li, Z., Li, P.-Z. & Zhao, Y. Linking nitrogen-rich organic cages into isoreticular covalent organic frameworks for enhancing iodine adsorption capability. *ACS Materials Lett.* **5,** 1546-1555 (2023).
29. Yuan, C. et al. Crystalline C-C and C=C bond-linked chiral covalent organic frameworks. *J. Am. Chem. Soc.* **143**, 369-381 (2021).
30. An, S. et al. Construction of covalent organic frameworks with crown ether struts. *Angew. Chem. Int. Ed.* **60,** 9959-9963 (2021).
31. Ma, T. et al. Signel-crystal x-ray diffraction structures of covalent organic frameworks. *Science* **361,** 48-52 (2018)
32. Shen, J. et al. A rings-in-pores net: crown ether-based covalent organic frameworks for phase-transfer catalysis. *Chem. Commun.* **56,** 595-598, (2020).
33. Yuan, L., Zhu, J. Wu, S. & Chi. C. Enhanced emission by stacking of crown ether side chains in a 2D covalent organic framework. *Chem. Commun.* **58,** 1302-1305, (2022).
34. Sasmal, H., S., Kumar M., A., Majumder, P. & Banerjee, R. Landscaping covalent organic framework nanomorphologies. *J. Am. Chem. Soc.* **144**, 11482-11498 (2022).
35. Matsumoto, M. et al. Rapid, Low Temperature Formation of Imine-Linked Covalent Organic Frameworks Catalyzed by Metal Triflates. *J. Am. Chem. Soc.* **139**, 4999-5002 (2017).
36. Li, Q. et al. Two-dimensional MXene-polymer heterostructure with ordered in-plane mesochannels for high-performance capacitive deionization. *Angew. Chem. Int. Ed.* **60**, 26528-26534 (2021).

37. Meng, Q. W. et al. Enhancing ion selectivity by tuning solvation abilities of covalent-organic-framework membranes. *PNAS* **121**, e2316716121 (2024).
38. Frensdorff, H. K. Stability constants of cyclic polyether complexes with univalent cations. *J. Am. Chem. Soc.* **93,** 600-606 (1971).
39 Kumpr, R. A. & Dougherty, D. A. A mechanism for ion selectivity in potassium channels: Computational studies of cation-π interactions. *Science* **261,** 1708-1710 (1993).
40. Gallivan, J. P. & Dougherty, D. A. A computational study of cation π interactions vs salt bridges in aqueous media implications. *J. Am. Chem. Soc.* **122,** 870-874 (2000).
41. Hayamizu, K., Chiba, Y. & Haishi, T. Dynamic ionic radius of alkali metal ions in aqueous solution: a pulsed-field gradient NMR study. *RSC Adv.* **11**, 20252-20257 (2021).
42. Ahlrichs, R., Bär, M., Häser, M., Horn, H. & Kölmel, C. Electronic structure calculations on workstation computers: The program system turbomole. *Chem Phys Lett* **162,** 165–169 (1989).
43. Balasubramani, S. G. et al. Turbomole: Modular program suite for Ab initio quantum-chemical and condensed-matter simulations. *J. Chem. Phys.* **152,** 184107 (2020).
44. Perdew, J. P., Burke, K. & Ernzerhof, M. Generalized gradient approximation made simple. *Phys. Rev. Lett.* **77,** 3865–3868 (1996).
45. Grimme, S., Ehrlich, S. & Goerigk, L. Effect of the damping function in dispersion corrected density functional theory. *J. Comput. Chem.* **32,** 1456–1465 (2011).
46. Weigend, F. & Ahlrichs, R. Balanced basis sets of split valence, triple zeta valence and quadruple zeta valence quality for H to Rn: Design and assessment of accuracy. *Phys. Chem. Chem. Phys.* **7,** 3297–3305 (2005).
47. Becke, A. D. Density-functional thermochemistry. III. The role of exact exchange. *J Chem Phys.* **98,** 5648–5652 (1993).
48. Lee, C., Yang, W. & Parr, R. G. Development of the colle-salvetti correlation-energy formula into a functional of the electron density. *Phys. Rev. B* **37,** 785–789 (1988).
49. Vosko, S. H., Wilk, L. & Nusair, M. Accurate spin-dependent electron liquid correlation energies for local spin density calculations: A critical analysis. *Can. J. Phys.* **58,** 1200–1211 (1980).
50. Stephens, P. J., Devlin, F. J., Chabalowski, C. F. & Frisch, M. J. Ab initio calculation of vibrational absorption and circular dichroism spectra using density functional force fields. *J. Phys. Chem.* **98,** 11623–11627 (1994).
51. Klamt, A. & Schüürmann, G. COSMO: A new approach to dielectric screening in solvents with explicit expressions for the screening energy and its gradient. *J. Chem. Soc. Perkin Trans.* 2 **5,** 799–805 (1993).
52. Carvalho, N. F. & Pliego, J. R. Cluster-continuum quasichemical theory calculation of the lithium ion solvation in water, acetonitrile and dimethyl sulfoxide: An absolute single-ion solvation free energy scale. *Phys. Chem. Chem. Phys.* **17,** 26745–26755 (2015).
53. Abraham, M. J. et al. GROMACS: High performance molecular simulations through multi-level parallelism from laptops to supercomputers. *SoftwareX* **1–2,** 19–25 (2015).
54. Jorgensen, W. L., Chandrasekhar, J., Madura, J. D., Impey, R. W. & Klein, M. L. Comparison of simple potential functions for simulating liquid water. *J. Chem. Phys.*

79, 926–935 (1983).

55. Jorgensen, W. L., Maxwell, D. S. & Tirado-Rives, J. Development and testing of the OPLS all-atom force field on conformational energetics and properties of organic liquids. *J. Am. Chem. Soc.* **118,** 11225–11236 (1996).
56. Yabe, M., Mori, K., Ueda, K. & Takeda, M. Development of PolyParGen software to facilitate the determination of molecular dynamics simulation parameters for polymers. *Journal of Computer Chemistry, Japan -International Edition* **5,** 2018-0034 (2009).
57. Dodda, L. S., Cabeza de Vaca, I., Tirado-Rives, J. & Jorgensen, W. L. LigParGen web server: an automatic OPLS-AA parameter generator for organic ligands. *Nucleic Acids Res.* **45,** W331–W336 (2017).
58. Jorgensen, W. L. & Tirado–Rives, J. Molecular modeling of organic and biomolecular systems using BOSS and MCPRO. *J. Comput. Chem.* **26,** 1689–1700 (2005).
59. Darden, T., York, D. & Pedersen, L. Particle mesh ewald: An $N \cdot \log(N)$ method for Ewald sums in large systems. *J. Chem. Phys.* **98,** 10089–10092 (1993).
60. Essmann, U., Perera, L., Berkowitz, M. L., Darden, T., Lee, H. & Pedersen, L. G. A smooth particle mesh Ewald method. *J. Chem. Phys.* **103,** 8577–8593 (1995).
61. Bussi, G., Donadio, D. & Parrinello, M. Canonical sampling through velocity rescaling. *J. Chem. Phys.* **126,** 014101 (2007)
62. Bernetti, M. & Bussi, G. Pressure control using stochastic cell rescaling. J. Chem. Phys. 153, 114107 (2020).
63. Hess, B., Bekker, H., Berendsen, H. J. C. & Fraaije, J. G. E. M. LINCS: A linear constraint solver for molecular simulations. *J. Comput. Chem.* **18,** 1463–1472 (1997).